Evaluation of bioactivity of alkali- and heat-treated titanium using fluorescent mouse osteoblasts

Masako Tsukanaka(1), Koji Yamamoto(1), Shunsuke Fujibayashi(1), Deepak K. Pattanayak (2), Tomiharu Matsushita(2), Tadashi Kokubo(2), Shuichi Matsuda(1), Haruhiko Akiyama(1),

(1) Department of Orthopaedic Surgery, Graduate School of Medicine, Kyoto University Shogoin, Kawahara-cho 54, Sakyo-ku, Kyoto 606-8507, Japan

(2) Department of Biomedical Sciences, College of Life and Health Sciences, Chubu University, Matsumoto-cho 1200, Kasugai, Aichi 487-8501, Japan

H.Akiyama

Department of Orthopaedic Surgery, Graduate School of Medicine, Kyoto University Shogoin, Kawahara-cho 54, Sakyo-ku, Kyoto 606-8507, Japan

Tel.: +81 75 751 3365; fax: +81 75 751 8409.

E-mail address:hakiyama@kuhp.kyoto-u.ac.jp

Abstract

Stimulation of osteoblast proliferation and differentiation is important to the *in vivo* bone-bonding ability of biomaterials. Previous *in vitro* studies have used biochemical assays to analyze osteoblast-specific gene expression in cultured osteoblasts. In this study, we generated transgenic mice harboring a monomeric red fluorescent protein 1 transgene under the control of a 2.3-kb fragment of the *Col1a1* promoter, which is active specifically in osteoblasts and osteocytes. We established a fluorescent primary osteoblast culture system to allow noninvasive observation of osteoblast proliferation and differentiation on opaque materials *in vitro*. We used this system to evaluate alkali- and heat-treated titanium, which has a strong bone-bonding ability *in vivo*, and we observed a rapid increase in fluorescence intensity and characteristic multifocal nodule formation. A cell proliferation assay and RT-PCR to examine osteoblast-specific gene expression showed increased osteoblast proliferation and differentiation consistent with the fluorescence observations. This mouse model allowed us to use fluorescence intensity to visualize and quantify *in vivo* newly formed bone around implanted materials in femurs. The use of these fluorescent osteoblasts is a promising method for simple screening of the bone-bonding ability of new materials.

Introduction

Various biomaterials are available for joint implants, bone substitutes, and fixation devices. Many alloys and surface treatments have been developed to improve their affinity with bone tissue. The bone-bonding ability of these biomaterials is usually evaluated using animal experiments in which the biomaterial of interest is implanted into bones of large animals, such as dogs and rabbits, and the bonding force is measured mechanically using a detaching test [1] and the material-bone interface is evaluated histologically. In practical terms, large animal experiments are the most valid method for predicting outcomes in humans. However, because of the high cost of the animals, long experimental periods, and time-consuming assay procedures, such models are not ideal for screening a large number of new biomaterials.

To overcome these problems, *in vitro* methods have been introduced to measure proliferation and osteoblastic differentiation of cultured cells on biomaterials. However, there remain several drawbacks. First, to evaluate osteoblastic differentiation by analyzing osteoblast-specific marker genes and protein levels, cell cultures need to be stopped at each examination time point, and this hampers time-lapse observations of the same sample. Second, the cultured cells do not differentiate uniformly on the material of interest, and the positional information is inevitably lost by homogenization of the cells

to extract proteins and mRNA. Third, because most biomaterials are not translucent, cells growing on the material cannot be visualized using standard light microscopy. Fourth, most of the biochemical assay procedures are cumbersome and require many reagents and complex equipment, which introduce the potential risk of contamination and technical errors.

In this study we established a new evaluation system to: 1) simplify the *in vitro* assay procedure to facilitate high-throughput screening and 2) enable serial evaluation of cell differentiation on the same metal sample without losing positional information.

Fluorescent proteins are used widely in noninvasive imaging of living cells. Fluorescence imaging systems are useful in the field of biomaterial evaluation because the opacity and the surface roughness of most biomaterials prevent the use of light microscopy to obtain focused images. High-resolution images from selected depths can be obtained using fluorescence bioimaging with a confocal laser scanning microscope. Several applications of fluorescence bioimaging technology for biomaterial evaluation have been reported. Blum et al. used a rat fibroblastic cell line transfected by retroviral vectors harboring enhanced green fluorescent protein (eGFP) and luciferase expressed through the cytomegalovirus promoter to visualize cells seeded in a hydrogel material and on titanium fiber mesh [2]. Xia et al. visualized cell survival in scaffolds after *in*

vivo implantation of human mesenchymal stem cells transfected by retroviral vectors encoding eGFP [3]. These methods are useful for evaluating cell shapes and numbers on materials but they do not provide information about the differentiation status of the cells. To visualize the differentiation of cells grown on biomaterials, it is necessary to restrict the expression of fluorescence to specific stages of cell differentiation.

The 2.3-kb fragment of the promoter of *Col1a1* is an osteoblast-specific promoter, which was reported by Dacic et al. [4] to become active specifically in differentiated osteoblasts and osteocytes [5]. In this study, we generated transgenic mice harboring a monomeric fluorescent protein 1 (*mRFP1*) transgene under the control of the *Col1a1* 2.3-kb promoter (*Col1a1(2.3kb)–mRFP1* mice). Using calvarial osteoblasts harvested from this mouse line, we established a primary osteoblast culture system to visualize osteoblast differentiation on biomaterials.

To validate this system using fluorescent osteoblasts, we evaluated alkali- and heat-treated titanium as a positive control because this surface treatment improves the bone-bonding ability of titanium metal. We have reported excellent bone-bonding ability with this treatment evaluated by mechanical tests using large animals [6] and favorable clinical outcomes of hip implants that have received this treatment [7].

Enhanced osteoblastic differentiation of osteoblasts on titanium plates after alkali- and heat- treatment has been reported by Isaac et al. [8].

By analyzing the fluorescent images obtained longitudinally from the same samples, we quantified fluorescence as an indicator of gene expression and the development of mineralized nodules. This system revealed a rapid increase in fluorescence intensity and a characteristic multifocal developmental pattern of calcified nodules in cells grown on alkali- and heat-treated titanium plates. We performed *in vivo* evaluations of alkali- and heat-treated titanium used in transgenic mice, and we obtained similar results to those obtained from our *in vitro* evaluation. This is the first report to show: 1) the *in vitro* and *in vivo* use of a fluorescence bioimaging system established from transgenic mice harboring an *mRFP1* transgene under the control of the osteoblast specific 2.3-kb fragment of the *Col1a1* promoter for biomaterial evaluation and 2) the pattern of longitudinal nodule development on biomaterials using images obtained noninvasively from the same samples.

Materials and methods

Preparation of titanium materials

Commercially pure (99.5%) titanium (CpTi) plates (Nilaco Co., Tokyo, Japan)

were cut to the sizes of 18 × 18 × 1 mm for 6-well culture plates and 14 × 14 × 1 mm

for 12-well culture plates, and the titanium plates were polished with number 400

diamond plate. Alkali- and heat-treated titanium (AhTi) samples were produced as

described previously [6]. Briefly, titanium plates were soaked in 5 M NaOH at 60 °C for

24 h and subsequently heated at 600 °C for 1 h. The previously reported mean average

surface roughness (Ra) and maximum roughness (Rmax) of the titanium plates were

0.32 and 3.63 μm for CpTi, 0.35 and 4.13 μm for AhTi, respectively [9]. For *in vivo*

experiments, pure titanium wires with a diameter of 0.6 mm (Nilaco Co.) were used. All

samples were sterilized in ethylene oxide gas before use. Photographs of these materials

are shown in Figure 1a and 1b.

Scanning electron microscopy

The materials were observed using a field-emission scanning electron

microscope (SEM) (S-4700; Hitachi Ltd., Tokyo, Japan) at an acceleration voltage of 5

kV. The SEM images of the samples are shown in Figure 1c–h. To observe the cells on

the materials, 2 days after seeding mouse calvarial osteoblasts on CpTi and AhTi plates,

the cells were fixed in 2% glutaraldehyde for 1 h. The plates were rinsed gently with 0.1

M phosphate buffer at pH 7.2, dehydrated in an ethanol series, frozen in tert-butyl

alcohol, freeze-dried, and sputter-coated with gold and palladium.

Animals

C57BL/6 transgenic mice harboring the *mRFP1* gene under the control of the 2.3-kb *Col1a1* promoter fragment (*Col1a1(2.3 kb)–mRFP1* mice) were created (Figure 2a). Genotyping was performed by PCR using the primers 5′-TCCCCGACTACTTGAAGCTG-3′ and 5′-CTTGGCCATGTAGGTGGTCT-3′, which amplify 317 bp of *mRFP1* (Figure 2b). The animal care and experimental procedures used were approved by the Animal Research Committee, Kyoto University, and were performed according to the Regulation on Animal Experimentation at Kyoto University.

Cell culture

Primary mouse calvarial osteoblasts were harvested from the calvaria of 1- to 5-day-old neonatal transgenic mice using a modification of a previously described protocol [10]. Calvarial bone fragments were subjected to five sequential 15 min digestions in medium containing 0.1% collagenase P (Roche Applied Science, Indianapolis, IN, USA) and 0.00125% trypsin (Sigma-Aldrich, St. Louis, MO, USA),

and cell fractions 3–5 were collected. Cells were seeded at a density of 3×10^5 and 1×10^5 cells/well in 6- and 12-well tissue culture polystyrene plates, respectively, containing the titanium plates on the bottom. Cells were grown in osteogenic medium comprising DMEM (Sigma-Aldrich) supplemented with 10% fetal bovine serum (Tissue Culture Biologicals, Long Beach, CA, USA), 10 mM β-glycerophosphate (Sigma-Aldrich), 80 μg/ml ascorbic acid (Sigma-Aldrich), and 10^{-8} M dexamethasone (Sigma-Aldrich) at 37 °C in a humidified atmosphere of 5% CO_2 and 95% air. The culture medium was replaced every other day.

Confocal laser scanning imaging of cell cultures

Fluorescence imaging of cultured cells was performed every 4 days after seeding until day 28. Fluorescence images were obtained with a confocal laser microscope (Nikon Instruments Inc., Tokyo, Japan). mRFP1 was excited using a 543 nm laser and detected through a 590/50 nm band-pass filter. For each sample, one low magnification (2×) field image and nine high magnification (10×) field images were captured in 512×531 pixels. The experiment was repeated three times, and the pinhole setting and contrast gain were maintained for all scans at the same magnifications. The images were analyzed using NIH ImageJ free software available at

9

http://rsb.info.nih.gov/nih-image/. The number of red pixels was counted in each sample.

The threshold was maintained for all images. The intensity of mRFP1 expression (total

fluorescent area) was defined as the total number of red pixels from nine

high-magnification (10×) fields. Red fluorescent spots of >10 pixels in

low-magnification images (2×) were considered to be calcification nodules, and the

number and the size of nodules were analyzed using the "Analyze Particle" function of

ImageJ.

2,3-Bis(2-methoxy-4-nitro-5-sulfophenyl)-2H-tetrazolium-5-carboxanilide   (XTT)

reduction assay

To measure cell number 2, 7 and 16 days after seeding, an XTT (2,3-Bis(2-

methoxy-4-nitro-5-sulfophenyl)-2H-tetrazolium-5-carboxanilide) reduction assay was

performed as described previously [11]. Briefly, 500 µl of XTT working solution was

added to each well, the cells were incubated at 37 °C for 6 h, and the absorbance was

measured on a microplate reader (Thermo LabSystems, Cheshire, UK). Specific

absorbance was calculated as follows: specific absorbance = A450 nm (test) – A450 nm

(blank) – A630 nm (test).

RT-PCR

Total RNA was extracted using the RNAeasy Mini Kit (Qiagen, Hilden, Germany) according to the manufacturer's instructions. The quality of RNA was confirmed by electrophoresis using an agarose ethidium bromide gel. From each sample, 200 ng of RNA was reverse-transcribed with random primers using the Transcriptor First Strand cDNA Synthesis kit (Roche Applied Science). Real-time PCR was performed to assess the expression levels of the genes type I collagen (*Col1a1*), osteocalcin (*Ocn*), and alkaline phosphatase (*Alp*) using the carousel-based LightCycler system (Roche) with FastStart DNA Master SYBR Green (Roche). The primers were as follows: *glyceraldehyde 3-phosphate dehydrogenase* (*Gapdh*), 5′-TGTCCGTCGTGGATCTGAC-3′ and 5′-CCTGCTTCACCACCTTCTTG-3′; *Alp*, 5′-ACTCAGGGCAATGAGGTCAC-3′ and 5′-CACCCGAGTGGTAGTCACAA-3′; *Col1a1*, 5′-CTCCTGGCAAGAATGGAGAT-3′ and 5′-AATCCACGAGCACCCTGA-3′; and *Ocn*, 5′-AGACTCCGGCGCTACCTT-3′ and 5′-CTCGTCACAAGCAGGGTTAAG-3′.

Surgical procedure

Ten-week-old male *Col1a1(2.3 kb)–mRFP1* mice were anesthetized by

11

intraperitoneal injection of pentobarbital sodium (40 mg/kg). The lateral thigh and knee

joint were incised, and the knee joint was opened by medially dislocating the patella. A

hole was drilled into the intercondylar fossa with a 23-G needle, and a treated or

untreated titanium wire was tapped from the hole into the medullary cavity until it broke

through the cortex of the greater trochanter. Both ends of the wire were bent and

trimmed, and the knee joint and skin were sutured after reducing the patella.

Imaging of mRFP1 fluorescence of the intramedullary wires

Mice were sacrificed 28 days after the implantation. The distally protruding

wire was cut and the rest of the wire was pulled out proximally. From the distally cut

end, 2 mm was excluded, and the remaining 8 mm was set as the region of interest.

Fluorescence images were obtained just after wire removal using a stereomicroscope

(SZX12; Olympus, Tokyo, Japan) equipped with a fluorescent lamp system with the

same conditions and exposure time. For each wire, the entire circumference was

captured in two images taken from the top and the bottom. The number of red pixels on

the wire was counted.

Histological examination

Twenty-eight days after implantation, the mice were sacrificed and the right femur was removed and fixed in 10% phosphate-buffered formalin (pH 7.25) for 7 days and dehydrated in an ethanol series. The specimens were then embedded in EpoFix Resin (Struers, Ballerup, Denmark) and cut with a band saw (BS-3000CP; EXACT cutting system, Norderstedt, Germany) perpendicular to the longitudinal axis of the femur. For each sample, three sections were chosen (subtrochanteric, middle shaft, and supracondylar regions). The sliced samples were ground to a thickness of 40–60 μm using a grinding–sliding machine (microgrinding MG-4000; EXACT). The sections were stained with Van Gieson's picrofuchsin [12]. The ratio of bone contact relative to the total perimeter of the implant was defined as the affinity index and was quantified using ImageJ.

Statistical analysis

The data are presented as the mean ± SD and were assessed using Student's *t* test to compare two groups. Differences with $p < 0.05$ were considered significant.

Results

Specific expression of red fluorescence was observed *in vivo* in bone tissues and *in vitro* in differentiated osteoblasts

To verify the tissue specificity of mRFP1 expression, fluorescent images were obtained in neonatal mice. Images of forelimbs of a 7-day-old transgenic mouse using light and fluorescence microscopy are shown in Figure 2c. Red fluorescence in the limb skeleton was observed through the skin of the transgenic mouse. The calvarial bone showed a high level of expression of mRFP1 (Figure 2d). Each osteoblast was visualized in the calvaria using a confocal laser microscope (Figure 2e and 2f). Macrofluorescence photography and observations of frozen sections of an exposed femur of a 3-week-old transgenic mouse showed no fluorescence in the growth plate and articular cartilage (Figure 2g and 2h). The sustained expression of mRFP1 was confirmed in a 10-month-old transgenic mouse (Figure 2i).

To confirm this transgene expression in culture, cultured osteoblasts were observed with fluorescence imaging. Figures 2j and 2k show images obtained using light and fluorescence microscopy to observe cultured osteoblasts in a polystyrene culture dish on day 16. Red fluorescence was observed mainly in areas dense with osteoblasts. Serial observation of osteoblasts on titanium plates using a confocal microscopy showed that fluorescence became detectable around culture day 7 and the

fluorescent area increased progressively over time (Figure 2l).

Osteoblasts grown on AhTi plates expressed red fluorescence in a larger area throughout the observation period compared with those grown on CpTi plates

To visualize the time course and spatial distribution of osteoblast proliferation and differentiation on the biomaterials used in this culture system, serial images of the same sample sets were obtained over 4 weeks (Figure 3a). As shown in Figure 3b, the fluorescent area began to increase on culture day 16 on both materials. The fluorescent area on day 16 was three-times larger on AhTi plates ($1.65 \times 10^5 \pm 3.87 \times 10^4$ pixels) compared with CpTi plates ($4.39 \times 10^4 \pm 4.45 \times 10^4$ pixels), and this difference continued throughout the observation period. However, the average daily increase in the total fluorescent area between day 16 to day 24 was 5.70×10^4 pixels/day for CpTi plates and 5.68×10^4 pixels/day for AhTi plates, which did not differ between materials.

Multifocal nodule formation was observed on AhTi plates

The nodule numbers counted as fluorescent spots in low-magnification images are shown in Figure 3c, and the average sizes of these nodules are shown in Figure 3d. On day 16, the nodule number was three times higher in the AhTi plates (66.7 ± 9.45)

than in the CpTi plates (17 ± 6.93) ($p < 0.05$). By contrast, the average nodule size was 1.5 times larger in the AhTi plates (110 ± 1.21) than in the CpTi plates (73.3 ± 061) ($p < 0.05$). To gain an overview of nodule development, the distribution of the sizes and numbers of nodules in a sample is shown in Figure 3e. There were more small nodules in the AhTi plate throughout of the observation period (Table 1). These results indicate that AhTi plates accelerated the onset of differentiation, but once the process had started, the progression was affected less by the treatment.

SEM observations, XTT assay, and RT-PCR showed increased proliferation and differentiation of osteoblasts on AhTi plates

SEM observations, XTT assays, and RT-PCR analysis were performed to relate the results obtained by fluorescence observations to known indicators of osteoblast proliferation and differentiation. SEM observations on culture day 2 showed favorable attachment of osteoblasts to both materials (Figure 4a). The morphology of the osteoblasts differed between materials: osteoblasts were large and flat on CpTi plates but small and rounded on AhTi plates. These differences in shape reflect differences in the surface characteristics of the materials. The results of the XTT analysis of cell number are shown in Figure 4b. On day 2, the mean absorbance was 60% higher for

AhTi plates ($0.201 \pm 0.0352/\text{cm}^2$) than for CpTi plates ($0.121 \pm 0.0393/\text{cm}^2$) ($p < 0.05$).

However, no significant difference was observed on day 7 and day 16, indicating that

AhTi treatment promoted cell adhesion and proliferation, which were related to the

accelerated onset of fluorescence expression on AhTi plates.

Osteoblast-specific gene expression levels were determined using RT-PCR on

days 2, 7, 14, and 16 (Figure 4c). *Alp* expression increased throughout the observation

period for cells grown on both materials. The cells on AhTi plates had a nonsignificantly

higher *Alp* expression level on day 7 ($p = 0.06$), day 14 ($p = 0.06$), and day 16 (p = 0.06)

compared with cells grown on CpTi plates. *Ocn* expression increased on day 14 for both

materials. These results are compatible with the finding that the fluorescence expression

driven by the *Col1a1* 2.3-kb promoter started increasing around day 16. Although the

expression levels were low, significantly higher *Ocn* expression levels were observed on

AhTi plates on day 2 ($p < 0.05$) and day 7 ($p < 0.05$) compared with those observed on

CpTi plates. *Col1a1* expression for both materials increased throughout the observation

period, but its expression did not differ significantly between CpTi and AhTi plates (day

2, $p = 0.51$; day 7, $p = 0.62$; day 14, $p = 0.27$; day 16, p = 0.79).

Bone formation around the materials was visualized and quantified in the *in vivo* system

Next, to assess the application of this system for *in vivo* evaluation of materials, we quantified the newly formed bone around the intramedullary materials in the fluorescence images. The gross appearance of the operative procedure and an x-ray image of the implanted wire are shown in Figure 5a and 5b. Twenty-eight days after implantation, the wires were removed and fluorescence images were obtained (Figure 5c). The fluorescent area was five times larger for the AhTi wires compared with the CpTi wires (Figure 5d). Newly formed bone was also quantified using the affinity indexes obtained from histological sections stained with Van Gieson's picrofuchsin (Figure 5e). The affinity index was 60% higher for AhTi wires (46.1% ± 22.9%) compared with CpTi wires (27.9% ± 33.5%). These results are compatible with the fluorescence observations (Figure 5f).

Discussion

Several noninvasive bioimaging techniques to visualize osteoblast differentiation have been reported. Bar et al. reported a bioluminescence imaging method to visualize differentiation of bone marrow-derived mesenchymal stem cells to osteoblasts in transgenic mice harboring the firefly luciferase gene under the control of the human osteocalcin promoter (*hOC*) [13]. They also reported the time course of the

expression of luciferase during *in vivo* skeletal development and bone repair. Expression

of the *hOC* promoter is restricted to fully differentiated osteoblasts. However, in the

field of material evaluation, a broader range of differentiation stages is preferable for

imaging, and bioluminescent imaging is inadequate for obtaining high-resolution

images. Kuhn et al. [5] reported a fluorescence imaging system to observe osteoblasts

from transgenic mice harboring the *GFP* transgene under the control of the 2.3-kb

fragment of the *Col1a1* promoter cultured on carbonated hydroxyapatite-coated disks.

In this study, we used mRFP1 instead of GFP because of its greater tissue penetration

and spectral separation from autofluorescence and other fluorescent proteins [14], which

enabled us to perform additional *in vivo* evaluation of the materials free of background

fluorescence. mRFP1 is a true monomeric variant of the red fluorescent protein DsRed

isolated from *Discosoma* sp. In contrast to DsRed, which is known to affect embryonic

stem cell development due to its obligate tetramerization [15], the safety of mRFP1 has

been well established. Transgenic mice with a ubiquitously high expression of mRFP1

have been reported to show no difference from their non-transgenic littermates in

embryonic development, adult organ maturation [16], and neural and muscular

functions [17]. The irradiation damage caused by a laser to induce fluorescence may be

of concern. However, scanning electron microscopic observation of cochleas stained

with fluorescent dyes after laser irradiation using confocal laser microscopy showed no

cellular or ultrastructural damage at a normal laser intensity [18]. Therefore, fluorescent

imaging using mRFP1 may be a suitable method for the non-invasive imaging of living

cells. Another report involved imaging of alkaline phosphatase activity using a

fluorinated ALP substrate detected with [19]fluorine magnetic resonance spectroscopic

imaging after hydrolysis [19]. Although this method is a useful noninvasive method to

visualize osteoblasts, it requires special reagents and analytical equipment.

Formation of a calcified extracellular matrix is an obvious indicator of osteoblast

maturation. Quantification of calcified nodules is often used to evaluate the *in vitro*

bone-bonding ability of biomaterials [20]. Several techniques for detecting nodules or

mineral deposition on opaque materials have been reported. They include histological

methods (von Kossa or Alizarin Red S staining), fluorescence labeling (tetracycline,

calcein blue, etc.) [21, 22], detection of the crystalline structure of calcium phosphate

using X-ray diffractometry, Fourier transform infrared spectrometry (FTIR) [23], and

scanning electron microscopy. [24, 25] Histological analysis is easy and has been used

for decades. However, except for FTIR, none of these techniques can distinguish

cell-mediated calcification from spontaneous precipitation of calcium phosphate in

degraded tissues. In this study, the fluorescent substance was produced by transgenic

mice, and the fluorescence detected from nodules definitely reflected cell-mediated calcification. Our method may be the first valid method for detecting cell-mediated calcification.

We performed serial observation of the same sample and found that materials with bone-binding ability showed multifocal development of nodules from the time of the initial formation but that the rate of the increase in size of the nodules did not differ between the materials. Maeda et al. [22] reported their noninvasive observations of nodule formation and quantified the time-dependent increase in green fluorescent emission from calcein-labeled nodules formed by rat mesenchymal stem cells cultured in osteogenic medium supplemented with calcein. However, they did not evaluate the characteristics of individual nodules. Our study is the first to quantify both the change in nodule number and average size with time in cells grown on biomaterials. We found a difference in the pattern of nodule formation between materials according to their bone-bonding ability. AhTi plates had accelerated growth and multifocal nodule formation. In large animal experiments, the application of alkali and heat treatment accelerates the increase in failure load in detaching tests [6].The failure load of alkali- and heat-treated implants was significantly higher than that of control titanium implants at four weeks. Although further studies on other bone-bonding biomaterials are required,

the acceleration of an increase in failure load *in vivo* may be explained by accelerated multifocal bone–material bonding, which is represented as multifocal nodule formation *in vitro*.

In this study, we also used fluorescence images to quantify new bone formation around the biomaterial *in vivo*. Compared with conventional histological evaluation, this technique is easy to perform and requires no sample preparation before observation. The bone-bonding ability of biomaterials has not been evaluated in transgenic animals with an introduced fluorescent marker gene. This may be because the genetics of large animals commonly used in biomaterial evaluation have not been well studied and gene-modified animals are not available. Although mice are too small to perform mechanical tests, our *in vivo* experimental model is useful for confirming the results of an *in vitro* culture system and may be a promising modality for the *in vivo* study of biomaterials.

Lastly, from the point of animal welfare, this system may help reduce the number of animals needed for experimental work. Evaluating the same sample repeatedly would require fewer samples and cells, and hence fewer neonatal mice. Establishment of an osteoblastic cell line from this transgenic mouse could reduce the number of experimental animals needed for research even further.

In conclusion, we performed noninvasive serial observations of osteoblast proliferation, differentiation, and nodule formation on biomaterials. This system may be a promising method for screening and studying the bone-bonding ability of biomaterials.

Acknowledgments

Conflict of interest

All other authors have no conflicts of interest.

References

1. Nakamura T, Yamamuro T, Higashi S, Kokubo T, Itoo S. (1985) A new glass-ceramic for bone replacement: evaluation of its bonding to bone tissue. J Biomed Mater Res 19:685-698

2. Blum JS, Temenoff JS, Park H, Jansen JA, Mikos AG, Barry MA. (2004) Development and characterization of enhanced green fluorescent protein and luciferase expressing cell line for non-destructive evaluation of tissue engineering constructs. Biomaterials 25:5809-5819

3. Xia Z, Ye H, Locklin RM, Ferguson DJ, Cui Z, Triffitt JT. (2005) Efficient characterisation of human cell-bioceramic interactions in vitro and in vivo by using enhanced GFP-labelled mesenchymal stem cells. Biomaterials 26:5790-5800

4. Dacic S, Kalajzic I, Visnjic D, Lichtler AC, Rowe DW. (2001) Col1a1-driven transgenic markers of osteoblast lineage progression. J Bone Miner Res 16:1228-1236

5. Kuhn LT, Liu Y, Advincula M, Wang YH, Maye P, Goldberg AJ. (2010) A nondestructive method for evaluating in vitro osteoblast differentiation on biomaterials using osteoblast-specific fluorescence. Tissue Eng Part C Methods 16:1357-1366

6. Yan WQ, Nakamura T, Kobayashi M, Kim HM, Miyaji F, Kokubo T. (1997) Bonding of chemically treated titanium implants to bone. J Biomed Mater Res 37:267-275.

7. Kawanabe K, Ise K, Goto K, Akiyama H, Nakamura T, Kaneuji A, Sugimori T,

Matsumoto T. (2009) A new cementless total hip arthroplasty with bioactive titanium porous-coating by alkaline and heat treatment: average 4.8-year results. J Biomed Mater Res B Appl Biomater 90:476-481

8. Isaac J, Galtayries A, Kizuki T, Kokubo T, Berda A, Sautier JM. (2010) Bioengineered titanium surfaces affect the gene-expression and phenotypic response of osteoprogenitor cells derived from mouse calvarial bones. Eur Cell Mater 20:178-196

9. Nishio K, Neo M, Akiyama H, Nishiguchi S, Kim HM, Kokubo T, Nakamura T. (2000) The effect of alkali- and heat-treated titanium and apatite-formed titanium on osteoblastic differentiation of bone marrow cells. J Biomed Mater Res 52:652-661

10. Wong GL, Cohn DV. Target cells in bone for parathormone and calcitonin are different: enrichment for each cell type by sequential digestion of mouse calvaria and selective adhesion to polymeric surfaces. (1975) Proc Natl Acad Sci U S A 72:3167-3171

11. Roehm NW, Rodgers GH, Hatfield SM, Glasebrook AL. (1991) An improved colorimetric assay for cell proliferation and viability utilizing the tetrazolium salt XTT. J Immunol Methods 142:257-265

12. Maniatopoulos C, Rodriguez A, Deporter DA, Melcher AH (1986) An improved method for preparing histological sections of metallic implants. Int J Oral Maxillofac

Implants Summer 1:31-37

13. Iris B, Zilberman Y, Zeira E, Galun E, Honigman A, Turgeman G, Clemens T, Gazit Z, Gazit D. (2003) Molecular imaging of the skeleton: quantitative real-time bioluminescence monitoring gene expression in bone repair and development. J Bone Miner Res 18:570-578

14. Campbell RE, Tour O, Palmer AE, Steinbach PA, Baird GS, Zacharias DA, Tsien RY. (2002) A monomeric red fluorescent protein. Proc Natl Acad Sci U S A 99:7877-7882

15: Hadjantonakis AK, Macmaster S, Nagy A. (2002) Embryonic stem cells and mice expressing different GFP variants for multiple non-invasive reporter usage within a single animal. BMC Biotechnol. 11;2:11.

16: Zhu H, Wang G, Li G, Han M, Xu T, Zhuang Y, Wu X. (2005) Ubiquitous Expression of mRFP1 in Transgenic Mice. Genesis 42:86–90

17: Long JZ, Lackan CS, Hadjantonakis AK. (2005) Genetic and spectrally distinct in vivo imaging: embryonic stem cells and mice with widespread expression of a monomeric red fluorescent protein. BMC Biotechnol. 4;5:20

18: Flock A, Flock B, Scarfone E. (1998) Laser scanning confocal microscopy of the hearing organ: fluorochrome-dependent cellular damage is seen after overexposure. J Neurocytol. 27, 507–51615.

19: Gade TP, Motley MW, Beattie BJ, Bhakta R, Boskey AL, Koutcher JA, Mayer-Kuckuk P. (2011) Imaging of alkaline phosphatase activity in bone tissue. PLoS One 6:e22608

20. Declercq HA, Verbeeck RM, De Ridder LI, Schacht EH, Cornelissen MJ. (2005) Calcification as an indicator of osteoinductive capacity of biomaterials in osteoblastic cell cultures. Biomaterials 26:4964-4974

21. Goto T, Kajiwara H, Yoshinari M, Fukuhara E, Kobayasi S, Tanaka T. (2003) In vitro assay of mineralized-tissue formation on titanium using fluorescent staining with calcein blue. Biomaterials 24:3885-3892

22. Maeda M, Hirose M, Ohgushi H, Kirita T. (2007) In vitro mineralization by mesenchymal stem cells cultured on titanium scaffolds. J Biochem. 141:729-736

23. Boyan BD, Bonewald LF, Paschalis EP, Lohmann CH, Rosser J, Cochran DL, Dean DD, Schwartz Z, Boskey AL. (2002) Osteoblast-mediated mineral deposition in culture is dependent on surface microtopography. Calcif Tissue Int 71:519-529

24. Stanford CM, Jacobson PA, Eanes ED, Lembke LA, Midura RJ. (1995) Rapidly forming apatitic mineral in an osteoblastic cell line (UMR 106-01 BSP). J Biol Chem 270:9420-9428

25. A. L. Boskey (2003) Mineral Analysis Provides Insights into the Mechanism of

Table1. Numbers of nodules smaller than 10^3 pixel

	day4	day8	day12	day16	day20	day24	day28
CpTi	0	0	1	7	23	49	72
AhTi	0	0	5	37	43	54	75

Figure legends

Fig. 1 Images of the materials.

a. Photograph of CpTi and AhTi plates for *in vitro* cell culture.

b. CpTi and AhTi wires for *in vivo* experiments.

c. Scanning electron microscope (SEM) image of the surface of a CpTi plate.

d. High-magnification image showing the smooth surface of a CpTi plate.

e. SEM image of a CpTi wire.

f. Low-magnification image of the surface of an AhTi plate is similar to that of a CpTi

plate.

g. Submicron rough structures observed on an AhTi plate.

h. SEM image of an AhTi wire.

Fig. 2 Establishment of *Col1a1(2.3 kb)–mRFP1* transgenic mice.

a. The structure of the Col1a1–mRFP1 transgene is shown. The *mRFP1* transgene is

under the control of the 2.3-kb fragment of promoter of *Col1a1*.

b. Genomic PCR analysis of the *mRFP1* transgene.

c. mRFP1 expression was observed in the limb skeleton of a 7-day-old transgenic

mouse.

d. High expression of mRFP1 was observed in a calvarium of a 7-day-old transgenic

mouse.

e. Confocal fluorescence images of a calvarium.

f. Individual osteoblasts are visualized in a high-magnification image.

g. Fluorescence images of an extracted femur of a 3-week-old mouse.

h. Zoomed image of the white boxed area in the frozen section image shown in g.

i. Macro- and frozen-section fluorescence images of a 10-month-old transgenic mouse.

j. Microscopic image of cell culture on day 16.

k. mRFP1 was observed in the dense cellular area.

l. Serial observations of cultured osteoblasts grown on a titanium plate. Development of

nodules can be seen.

Fig. 3 Time-lapse observations of the fluorescence of osteoblasts cultured on CpTi and

AhTi plates and analysis of nodule formation.

a. Serial low-magnification images of a CpTi plate and an AhTi plate obtained by

confocal fluorescence microscopy. Scale bar, 500 μm.

b. Changes in total fluorescent area on CpTi and AhTi plates. Images were obtained by

time-lapse observations of the same sample ($n = 3$).

c. Changes in nodule numbers counted in low-magnification images.

d. Changes in average size of nodules. Data shown in b–d are mean ± SD. *; $p < 0.05$.

e. Distribution of the size and number of nodules in an individual sample.

Fig. 4 Evaluation of proliferation and differentiation of osteoblasts cultured on CpTi and

AhTi plates using conventional methods.

a. SEM images of osteoblasts cultured on a CpTi or AhTi plate on day 2. White

arrowheads indicate the cell body.

b. The results of XTT assay on culture days 2, 7, and 16 show greater proliferation of

cells grown on AhTi plates compared with those grown on CpTi plates on day 2 ($p <$

0.05).

c. Real-time RT-PCR analysis of *Col1a1*, *Alp*, and *Ocn* expression. Data are presented

as mean ± SD ($n = 4$), * $p < 0.05$. Fold changes are adjusted relative to *Gapdh*

expression.

Fig. 5 *In vivo* evaluation of CpTi and AhTi wires.

a. A sample wire was placed in the right femur of the mouse, the ends of the wire were

bent, and the skin was sutured over them.

b. X-ray image of an implanted wire.

c. Fluorescent images of extracted wires were obtained 28 days after implantation.

Zoomed images of white boxed areas of CpTi and AhTi plates are shown on the right

of each image.

d. Newly formed bone around the wires was detected as red spots and the areas were

measured ($n = 4$). AhTi wires showed significantly larger fluorescent areas compared

with CpTi wires ($p < 0.05$).

e. Cross-sectional slices of CpTi and AhTi wires implanted for 28 days in mouse femurs.

Zoomed images of yellow boxed areas are shown on the right. Bone tissue stained

red with Van Gieson's picrofuchsin is observed on the surface of the AhTi wire but

not on the CpTi wire.

f. Affinity indexes of CpTi and AhTi wires ($n = 4$). The affinity index was significantly

higher in the AhTi wires than in the CpTi wires ($p < 0.05$). Data are presented as mean $\pm$
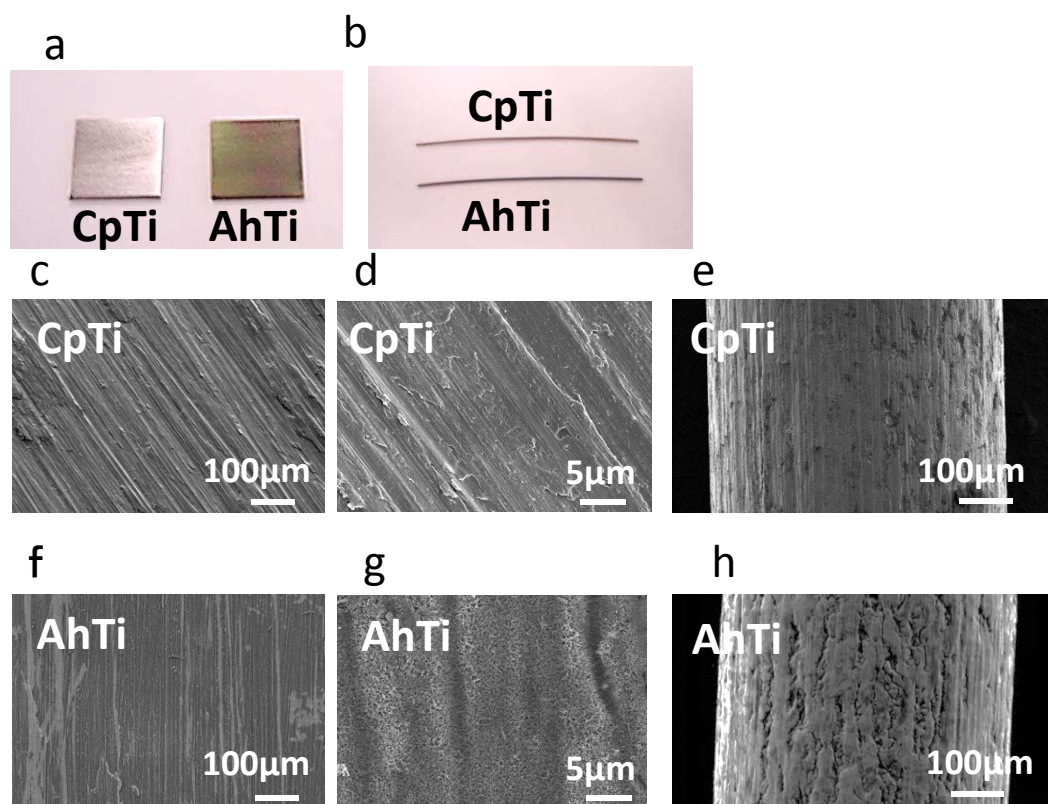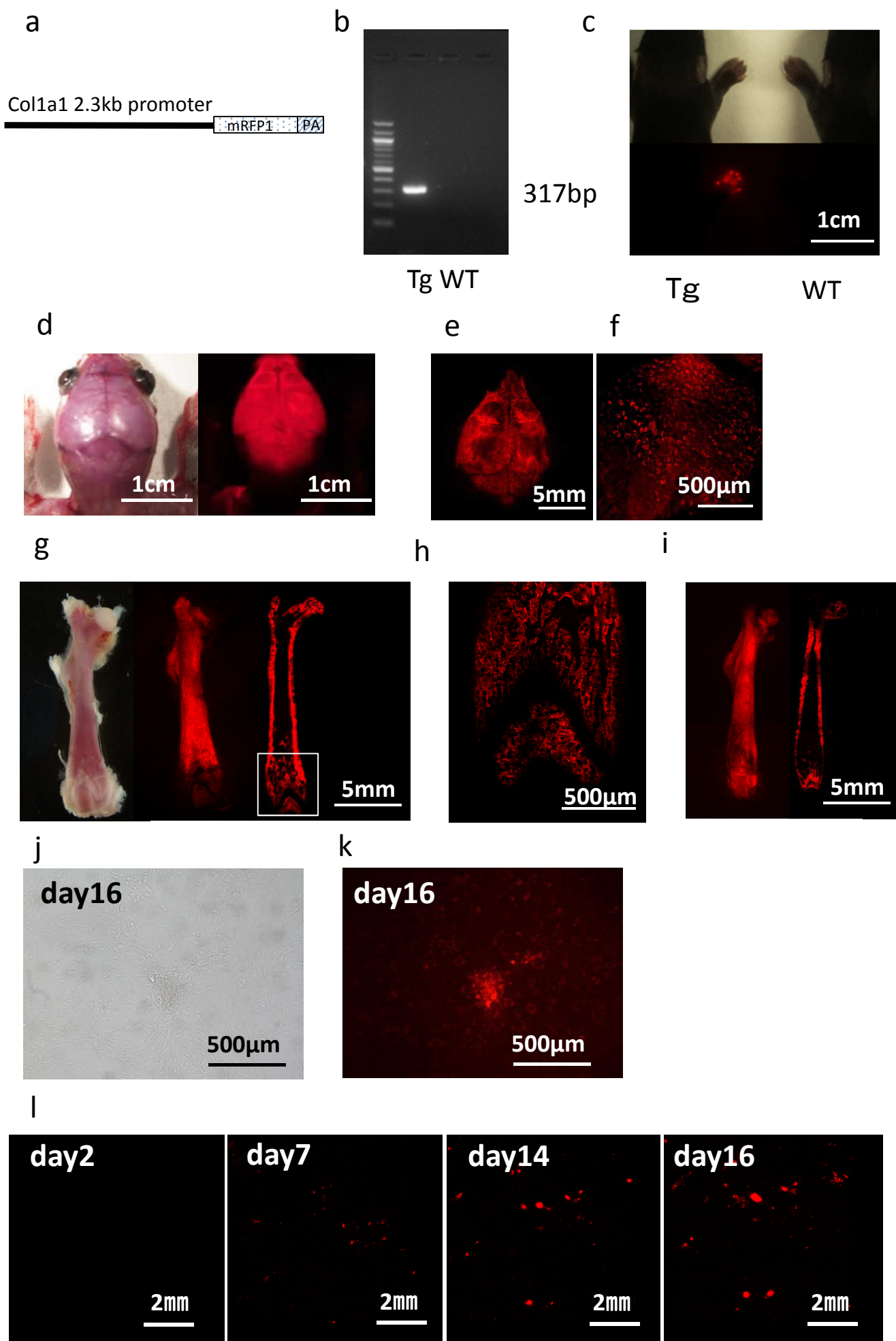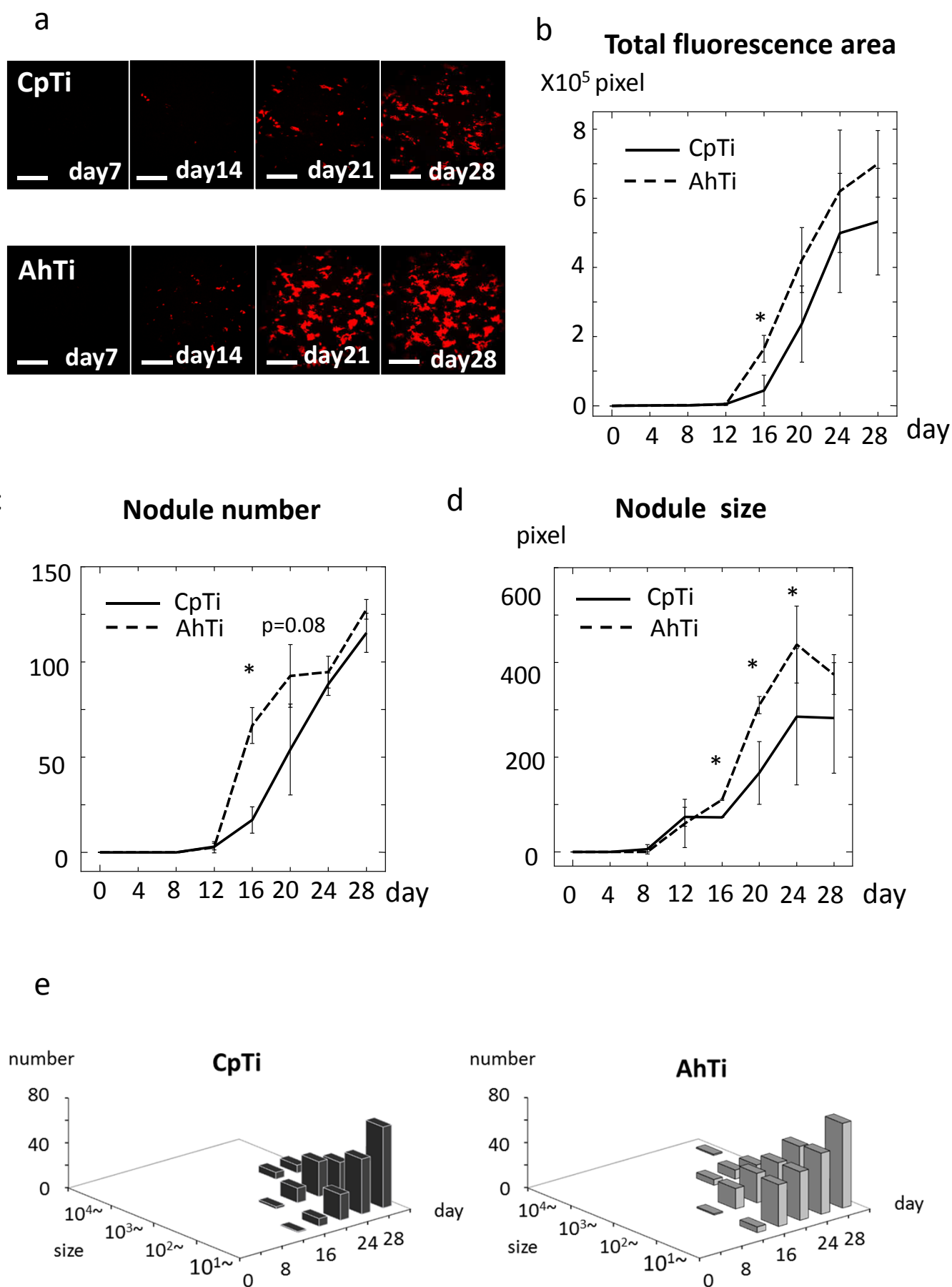
SD ($n = 4$), *; $p < 0.05$.

a

b

CpTi   AhTi

CpTi

AhTi

c

CpTi

100μm

d

CpTi

5μm

e

CpTi

100μm

f

AhTi

100μm

g

AhTi

5μm

h

AhTi

100μm

Figure 1.

a

Col1a1 2.3kb promoter
mRFP1 PA

b

317bp

Tg WT

c

1cm

Tg   WT

d

1cm   1cm

e

5mm

f

500µm

g

5mm

h

500µm

i

5mm

j

day16

500µm

k

day16

500µm

l

day2   day7   day14   day16

2mm   2mm   2mm   2mm

Figure 2.

a

CpTi — day7 — day14 — day21 — day28

AhTi — day7 — day14 — day21 — day28

b **Total fluorescence area**

X10^5 pixel

CpTi
AhTi

*

day

c **Nodule number**

CpTi
AhTi

p=0.08

*

day

d **Nodule size**

pixel

CpTi
AhTi

*

*

*

day

e

number

CpTi

size

day

number

AhTi

size

day

Figure 3.

Figure 4.

a

b

c

2mm 8mm

CpTi

AhTi

d

Fluorescence are

mm²

100

80

60

40

20

0

CpTi   AhTi

*

e

CpTi

AhTi

f

Affinity Index

%

80

60

40

20

0

CpTi   AhTi

*

Figure 5.